Received 3 April 2024; accepted 25 April 2024. Date of publication 29 April 2024; date of current version 6 August 2024.

Digital Object Identifier 10.1109/OJAP.2024.3394730

Point Cloud-Based Prediction Models of Dynamic Human Body Shadowing at 58 GHz

CHECHIA KANG[1] (Member, IEEE), XIN DU[2] (Member, IEEE), AND JUN-ICHI TAKADA[1] (Senior Member, IEEE)

[1]Department of Transdisciplinary Science and Engineering, Tokyo Institute of Technology, Tokyo 152-8550, Japan

[2]Graduate School of Sciences and Technology for Innovation, Yamaguchi University, Yamaguchi 755-8611, Japan

CORRESPONDING AUTHOR: C. KANG (e-mail: kang.c.aa@m.titech.ac.jp)

This work was supported by the Commissioned Research through the National Institute of Information and Communications Technology (NICT), Japan, under Grant JPJ012368C02701.

ABSTRACT As one of the channels used by the wireless gigabit (WiGig) protocol, a 58 GHz band has been deployed to realize a data rate of up to 100 gigabits per second (Gbps). Systems at the 58 GHz band point the main beam of the base station toward the mobile stations but suffer from a deep fading due to human body shadowing (HBS). To precisely predict the HBS channel considering the short wavelength at 58 GHz, a simulation method considering the detailed human geometry is needed. This paper proposes screen models and an elliptic cylinder model based on the instantaneous point clouds (PC) of human geometry for the HBS channel simulation using the uniform theory of diffraction (UTD). The proposals enable fair evaluation via a simultaneous measurement of the HBS channel and the PC. The HBS gains at the 58 GHz band in an indoor environment (6.5 m) between the measured and the simulated results based on the proposed models are compared. Compared with the conventional human model, the screen models are suitable for predicting the propagation channel cut-off by tracing the changing posture of the human body, and the elliptic cylinder model is suitable for predicting the shadowing distance by a 75% improvement.

INDEX TERMS Dynamic channel, human blockage model, millimeter wave propagation, UTD simulation.

I. INTRODUCTION

THE WIDE bandwidth availability at the millimeter wave (mmW) band enables the enhanced mobile broadband (eMBB) service. For example, the IEEE 802.11ay standard for wireless local area networks allows a throughput of 100 Gigabits-per-second (Gbps) at the license-free 58 GHz band (57.24 - 74.52 GHz) [1], [2]. Radio wave propagation at the 58 GHz band has more propagation loss compared with the frequency bands below 6 GHz due to the short wavelength. To compensate for the severe propagation loss, the directional antennas are used. In the mobile communication scenarios, the massive multi-input and multi-output (massive MIMO) base stations (BS) are developed to point the main beam of the array antenna toward the line-of-sight (LoS) channel between the BS and the mobile station (MS) [3].

However, as one of the main disadvantages, the LoS channel between the BS and the MS can be blocked easily by some dynamic objects, such as pedestrians and vehicles. When the first Fresnel zone of the LoS channel is blocked, the LoS channel fades and the communication cut-off occurs. Since the first Fresnel radius is proportional to the wavelength, even a human body can fully block the LoS channel at mmW band especially in the indoor scenario [4], [5]. Furthermore, the scintillation of the LoS channel occurs when there is a scattering path contributed by a dynamic object approaching the LoS path [6], [7].

To deal with the human body shadowing (HBS) problem, algorithms such as switching the communication channel to an alternative one before the shadowing event occurs, are attracting researchers' attention [8]. In [9], the handover scheme is determined by the human blockage with a motion capture (MoCap) camera. The prediction of the shadowing event was conducted by using the motion of the skeleton joints captured by the MoCap [10]. However, without

considering the occupation of the first Fresnel zone due to the human body, the throughput degradation can not be predicted correctly and the proactive network control suffers failures. Thus, the network engineers need a dynamic deterministic HBS channel model that can accurately predict the shadowing gain[1] based on the occupation of the first Fresnel zone.

The dynamic deterministic HBS channel is simulated based on the combination of the propagation model and a suitable instantaneous human body model. The HBS channel can be simulated accurately by using the combination of the full-wave methods, e.g., the finite-difference time-domain (FDTD) [11] method and the method of moment (MoM) [12], and the 3-dimensional (3D) human phantoms. In [13], the FDTD method and the voxel human model were used for dynamic wearable body area network (WBAN). Though the full-wave methods can consider the detailed shape of the 3D human phantoms, the escalating computational complexity proportional to the electrical size of the human body is not tolerable at the mmW band. Instead, high-frequency asymptotic models with simplified geometric human models are preferred. For example, the combination of the knife-edge diffraction-based (KED) method [14] with a vertical screen, the combination of the uniform theory of diffraction (UTD) method for wedge diffraction [15] with a prism-like model, and the combination of the UTD method for creeping diffraction [7], [16] with a circular or elliptic cylinder have been proposed. In previous research, the human body was modeled as a screen in [17], [18], a prism-like cylinder in [19], [20], and the circular and elliptic cylinders in [16]. All the conventional geometric human models were defined from the dimensions measured in advance.

The high-frequency asymptotic models should be validated by full-wave simulations or channel measurements. Though the result simulated by full-wave methods can be compared with the high-frequency asymptotic models directly, the computational complexity is not tolerable at the 58 GHz band, as mentioned above. On the other hand, channel measurements should match the position and the shape of the human specimen in the physic domain and the human body model for simulation. In conventional research, the human body model for simulation was shaped based on the pre-measured dimensions and positioned due to an estimation. The estimated position of the human body model was linearly related to the time domain by fixing the posture of the human specimen and letting the human specimen move at a fixed speed [21], [22]. In [21], the static object such as a metal plate was pulled on a rail system at a constant speed. In [22], The dynamic human body walked at a fixed speed with the help of a speed gun. The best fit of the geometries is found by sliding the time offset between the physical domain and the simulation.

[1]This paper deals with shadowing gain which is proportional to the signal strength, but it is obvious that the shadowing loss which is more commonly used is the inverse of the shadowing gain.

Due to the difficulty of letting the human specimen move at a constant speed, the difference between the positions of the human bodies in the simulation and the physical domain always exists. Since the HBS channel properties, especially the shadowing duration, are sensitive to the instantaneous clearance of the first Fresnel's zone, the human body model for simulation may lead to an inaccurate evaluation of the developed HBS channel models. To reconstruct the geometry in the simulation for accurate evaluation, marker-based and markerless MoCap systems are used. The marker-based MoCap recognizes the joints of the human skeleton by attaching the reflective markers on the skin of the human body, in [16], [18]. The geometric human models were reconstructed by skinning the human skeleton with screens or cylinders for the HBS channel simulation at the microwave band. However, the disagreement between the skin of the reconstructed models and the human body is intolerable for the HBS channel at the 58 GHz band. The markerless MoCap obtains the complex-shaped skin of the human body precisely as a point cloud (PC). Captured with light detection and ranging (LiDAR) or a markerless MoCap system, the PC represents the detailed surface of the propagation environment. The PC-based channel simulators have been developed for the static propagation environments in [23], [24], [25]. The reflection points on the walls and the ground were found by the PC and the normal vectors which calculated from the PC. The reflection and diffraction coefficients were then calculated by using geometrical optics and geometrical theory of diffraction (GO-GTD) [12]. However, due to the assumption of GO-GTD, conventional PC-based simulators do not suit the complex-shaped human body.

This research aims to develop a PC-based simulator for the shadowing gain that suits the dynamic HBS channel by applying the conventional UTD method for wedge diffraction and the proposed PC-based geometric human models. The proposed geometric human models change their shape at every moment to trace the time-varying shape of the human body. The flexible models take the detailed geometry of the human body into account to find the clearance of the first Fresnel zone at every moment and enable the simulation of dynamic HBS channels. To evaluate the proposals, a measurement of the dynamic propagation channel at 58 GHz shadowed by a human body using the synchronized channel sounder and MoCap system was conducted. To ensure an accurate evaluation, the PC of the human body is synchronized precisely to the instantaneous HBS channel by using the synchronized measurement system including a channel sounder and a MoCap system proposed by the authors [25]. The shadow distance, fading distance, and the pattern of the shadow gain simulated based on the proposed PC-based geometric human models are compared.

The remainder of this paper is organized as follows. In Section II, the proposed PC-based screen models and the elliptic cylinder models are described. In Section III, the validation of the proposed PC-based geometric models

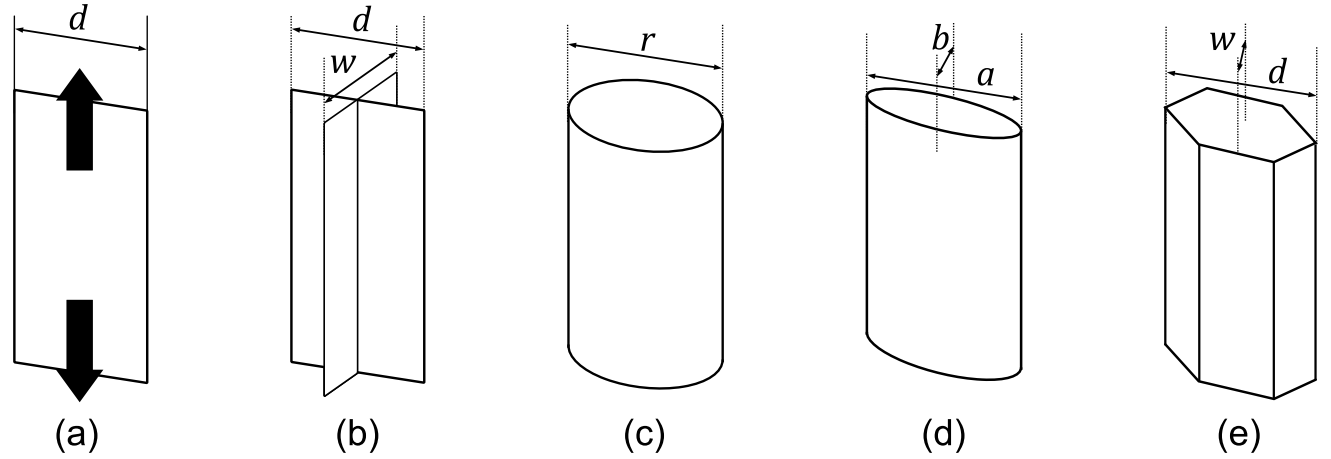

FIGURE 1. The geometric human models: (a) vertical screen [17], [18], [20], (b) double vertical screen [20], (c) circular cylinder [16], [19], [20], (d) elliptic cylinder [20], (e) hexagon prism [19]. Two PC-based vertical screen models and one elliptic cylinder model are proposed in this work.

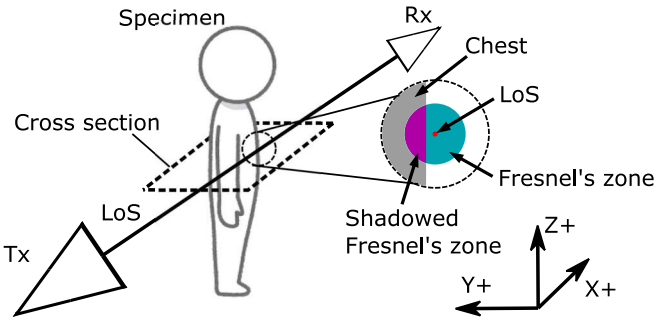

FIGURE 2. The clearance of the Fresnel zone shadowed by the belly of the human body. Because of the short wavelength at the mmW band, the clearance of the Fresnel zone can be considered as a 2D problem.

consists of the prediction methods of the HBS channel, the synchronized channel sounder and the MoCap, and the measurement setup and the specimen are explained. In Section IV, the comparison of measurement and simulation results for validating the proposed geometric models are presented. Finally, the conclusions are presented in Section V.

II. GEOMETRIC HUMAN MODELS

Considering a steady pedestrian motion across the LoS, as shown in Fig. 1, to predict the propagation channel, e.g., [16], [17], [18], [19], [20]. In the indoor scenario where the LoS path length is rarely longer than 10 m, the first Fresnel radius does not exceed 12 cm, which is small enough compared with a human's chest and arm. Thus, as shown in Fig. 2, the 3D shape of the human body can be approximated to a 2-dimensional (2D) human model, which is defined by the horizontal contour at the height where the LoS is closest to the human body. When the antennas are at the same height, the horizontal contour at the same height as the antennas is used. In this section, the PC-based geometric human models, the cross-section screen, the Bullington screen, and the cylinder model, are proposed. In Section II-A, the conventional fixed models are introduced, and the fixed screen model localized by measured PC is chosen as the reference to evaluate the proposed models, which change their shapes to fit the human body. Section II-B explains the processes to generate the proposed PC-based cross-section screen, Bullington screen, and the elliptic cylinder models from the instantaneous PC.

A. CONVENTIONAL FIXED MODELS LOCALIZED BY PC

Screen and cylinder models are the common shapes of the simplified human body in literature, as shown in Fig. 1, e.g., [16], [18], [19], [20]. In case a screen or a prism-like cylinder model is used in the propagation channel simulation, the double KED method or UTD method for wedge diffraction is used [18], [19], [20]. In case a circular or elliptic cylinder is used in the propagation channel simulation, the UTD method for creeping diffraction is used [16], [20]. The conventional model is defined with the dimensions of the human body measured in advance. However, regarding the shadowing gain calculated based on the cross-section of the human body from the antennas' viewpoint, the geometric human models with a fixed dimension suit only the specimen without any shape-changing during the measurement. Considering that shape change can never be eliminated, it can be expected that the conventional rigid screen model is not sufficient.

To validate the proposals, the conventional fixed screen model is chosen as the reference. The conventional fixed screen is defined based on the PC of the human body as follows. The face of the screen is normal to the LoS, the width of the screen is defined as the measured width of the corresponding part of the human body. For an accurate evaluation, the instantaneous position of the human body is found as the centroid of the contour of the captured point cloud, as shown in Fig. 3.

B. THE PROPOSED PC-BASED SCREEN MODELS

Regarding the changing cross-section of the human body walking with a natural gait, we propose three types of PC-based geometric models for the HBS simulation, i.e., the

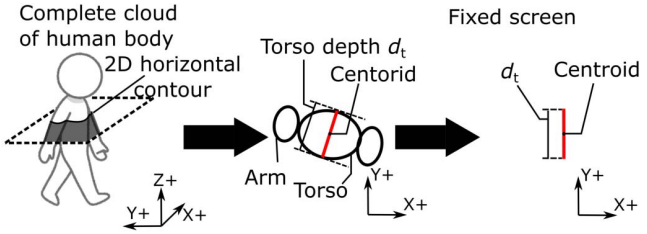

FIGURE 3. The process generating the rigid screen model from the complete PC of the human body. The 2D horizontal contour of the human body is formed by the points at the same height as the antennas. The parameters of the rigid screen, the width d_t and the center position p of the model, are found as the depth and the centroid of the contour.

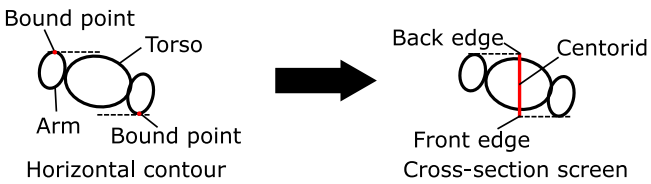

FIGURE 4. The process generating the Cross-section screen model. The coordinates in the direction perpendicular to the LoS of both edges are the same as the bound points in the same direction. The coordinates in the LoS direction are the same as the contour's centroid.

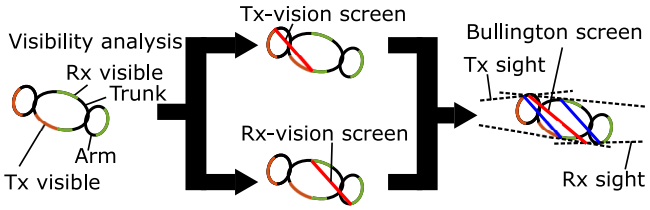

FIGURE 5. The process of generating the Bullington screen model. Firstly, the Tx-vision and the Rx-vision screens are defined by finding the bound points of the points visible to each antenna in the direction perpendicular to the LoS. Inspired by the Bullington model [26], the Bullington screen's edges are found at the intersection of the line drawn from both antennas to the edges of the two screens mentioned above.

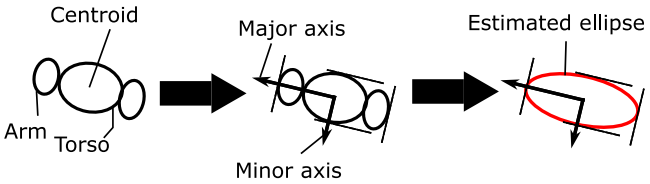

FIGURE 6. The process generating the elliptic cylinder model. The ellipse is defined by applying the principal component analysis to the contour related to its centroid. The major and the minor axes are found as the first and the second principal components. The sizes of both axes are found as the range of the points in the direction of both axes.

cross-section screen, the Bullington screen, and the elliptic cylinder. Among the three proposals, the cross-section screen is superior in computational simplicity, the Bullington screen considers the complex shape of the human body by visibility analysis, and the elliptic cylinder model takes the reflected wave from the human body into account.

1) CROSS-SECTION SCREEN

With the MoCap system synchronized to the channel sounder, the time-varying shape of the human body such as swinging arms can be taken into account. Here, we propose the cross-screen screen defined by the instantaneous circumference of the cross-section of the human body, as shown in Fig. 4. Keeping the face normal to the LoS, the position of the screen along the LoS is the same as the centroid of the horizontal contour of the human body. Positions of the edges are found as the bound points of the contour cloud in the same direction.

2) BULLINGTON SCREEN

Considering the edges of the cross-section screen may not be visible from the TRx due to the complex shape of the human body, the Bullington screen is defined based on the visibility of the contour points from the viewpoint of the TRx. First, the Tx-vision and Rx-vision screens are defined, as shown in Fig. 5. Positions of the edges of the Tx-vision screen and the Rx-vision screen are the positions of both bound points of the visible PC of the 2D contour along the direction perpendicular to the LoS. Then, inspired by the Bullington model [26], the Tx-vision screen and the Rx-vision screen are synthesized into the Bullington screen. The positions of the Bullington screen's edges are defined as the intersection of the lines drawn from the antennas to the edges of the Tx-vision screen and the Rx-vision screen.

3) ELLIPTICAL CYLINDER

Solid models such as circular and elliptical cylinders are used in [20], [25] to consider the effects of the interference due to the surface of the human body such as the creeping wave and the reflected wave, which are ignored by applying the screen models with the UTD method. Before and after the shadow event, the reflected waves from the surfaces additionally contribute to the received field [7], which enhances the small-scale fading. In the shadow region, the diffraction waves creeping along the surfaces lose more energy than diffracting around a wedge and lead to a deeper shadowing loss [27]. Compared with a circular cylinder, an elliptical cylinder is more similar to the shape of the human body and considers the direction of the human body in addition. The directions, sizes, and positions of the elliptic cylinder model are found by applying the principal component analysis (PCA) to the 2D horizontal contour related to the centroid of the contour, as shown in Fig. 6.

III. VALIDATION

In the dynamic HBS channel, the received power fluctuates and fades occasionally with the presence of the human body. To observe the dynamic propagation channel, the shadowing gain, $G^{\mathrm{S}}(t)$, is the instantaneous received power of the HBS channel relative to the LoS channel, which is calculated as

$$G^{\mathrm{S}}(t) = 10\log_{10}\frac{H(t)}{H^{\mathrm{LoS}}} \tag{1}$$

where $H(t)$ and H_{LoS} are the instantaneous HBS channel gain at time t and the static LoS channel gain, respectively.

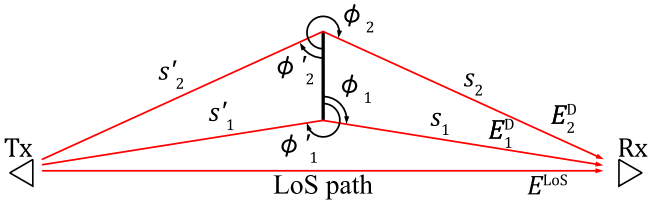

FIGURE 7. Diffraction from an absorbing half-plate located between the Tx and the Rx.

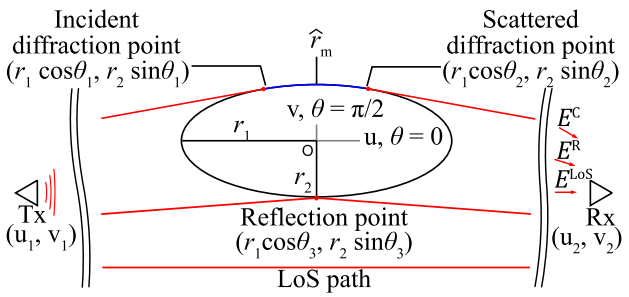

FIGURE 8. Diffraction from an ellipse located between the Tx and the Rx.

The channel gains are the ratio of the received power to the transmitted power.

To validate the proposed PC-based geometric models of the human body, the results of the propagation simulation using the proposals were compared with the measurement result in an indoor dynamic HBS scenario at 58 GHz band. In Section III-A, the prediction methods used in the simulation of the dynamic HBS channel are introduced. In Section III-B, the synchronized measurement system consists of the channel sounder at 58 GHz band and the MoCap is explained. In Section III-C, the details of the measurement in an indoor dynamic HBS scenario at 58 GHz are described.

A. PREDICTION METHODS

Since the power of a radio wave is in direct ratio to the square of its electric field, the simulated shadowing gain $G^{\mathrm{s}}_{\mathrm{sim}}(t)$ in the propagation simulations is calculated as

$$G^{\mathrm{s}}_{\mathrm{sim}}(t) = 10\log_{10}\frac{|E^{\mathrm{Rx}}(t)|^2}{|E^{\mathrm{LoS}}|^2} \tag{2}$$

where $E^{\mathrm{Rx}}(t)$ and E^{LoS} are the instantaneous received field at time t and the direct field, respectively. To validate the difference between the models of human bodies, the UTD method for edge diffraction [28] and the UTD for creeping diffraction [29] are chosen. The UTD method for edge diffraction is used for the screen models, and the UTD for creeping diffraction is used for the elliptical cylinder model. The 2D simulation is used for the sake of simplicity.

1) ABSORBING SCREEN UTD MODEL

The total received field from an infinite-long vertical screen $E^{\mathrm{Rx}}_{\mathrm{Screen}}$ is calculated as the summation of the diffraction fields from both sides of the screen and the direct field when the LoS is not blocked, and as only the summation of the diffraction fields when the LoS is blocked as

$$E^{\mathrm{Rx}}_{\mathrm{Screen}} = \begin{cases} G^{\mathrm{Tx}}G^{\mathrm{Rx}}E^{\mathrm{LoS}} + \sum_{i=1}^{2} G_i^{\mathrm{Tx}}G_i^{\mathrm{Rx}}E_i^{\mathrm{D}}, & (\mathrm{LoS}) \\ \sum_{i=1}^{2} G_i^{\mathrm{Tx}}G_i^{\mathrm{Rx}}E_i^{\mathrm{D}}, & (\mathrm{NLoS}) \end{cases} \tag{3}$$

where E_i^{D}, $G^{\mathrm{Tx,Rx}}$ and $G_i^{\mathrm{Tx,Rx}}$ are the electric fields of the diffraction paths from both edges of the screen, the antenna gains of the boresight and the directions toward the diffraction paths concerning the Tx and the Rx antennas, respectively.

The diffraction field E_i^{D} is calculated as

$$E_i^{\mathrm{D}} = E_0 H_0^{(2)}(k_0 s'_i) D_i \frac{e^{-\mathrm{j}k_0 s_i}}{\sqrt{s_i}} \tag{4}$$

where $E_0, H_0^{(2)}(.), k_0, s'_i, s_i$, and D_i are the electric field at source, the second kind of the Hankel function for the zeroth order, wave number in the free space, the distance from the Tx to the edge of the half-plane, the distance from the edge of the half-plane to the Rx, and the diffraction coefficient for the path i, respectively. The diffraction coefficient based on the UTD for absorbing half-plane diffraction is derived as

$$D_i = \frac{-e^{\frac{\mathrm{j}\pi}{4}}}{2\sqrt{2\pi k_0}}\sec\left(\frac{\varphi_i - \varphi'_i}{2}\right)F\left(2k_0L_i\cos^2\frac{\varphi_i - \varphi'_i}{2}\right) \tag{5}$$

where φ'_i and φ_i are the angles of incidence and diffraction measured from the edge, respectively, as shown in Fig. 7. The function $F(.)$ is the Fresnel integral calculated as

$$F(x) = \sqrt{x}e^{\mathrm{j}x}\int_{\sqrt{x}}^{\infty} e^{-\mathrm{j}t^2}\mathrm{d}t \tag{6}$$

where L_i is the distance factor calculated by (7).

$$L_i = \frac{s_i s'_i}{s_i + s'_i}. \tag{7}$$

By separating the diffraction wave via the wedge from the free space field in the LoS case, the UTD method for wedge diffraction can derive the Doppler frequency without repeatedly conducting the Fresnel integral.

2) ELLIPSE UTD MODEL

Consider a local coordinate system in the $u-v$ domain where the origin is the center of the ellipse and the major axis is the u axis, as shown in Fig. 8.

When the LoS is blocked by the obstacle, the diffraction wave creeps through the surface of the ellipse. The incident point and the diffraction point $(r_1\cos\theta_{1,2}, r_2\cos\theta_{1,2})$ are found on the ellipse as

$$\theta_{1,2} = \arcsin\frac{1}{\sqrt{\frac{u_{1,2}^2}{r_1} + \frac{v_{1,2}^2}{r_2}}} - \arctan\frac{u_{1,2}r_2}{v_{1,2}r_1} \tag{8}$$

where (u_1, v_1) and (u_2, v_2) are the coordinates of the Tx and Rx. $\theta_{1,2}$ are the parameters of the incident point and the scattered diffraction point, respectively.

To predict the creeping diffraction coefficient when the Rx is in the shadow region, the geodesic from the incident

diffraction point to the scattered diffraction point and the radii of the curvatures at both points are needed. The geodesic along an ellipse is the curve length $\widehat{r_m}$, which is derived as

$$\widehat{r_m} = r_2\left(\mathrm{E}\left(\theta_2|1-\frac{r_1^2}{r_2^2}\right)-\mathrm{E}\left(\theta_1|1-\frac{r_1^2}{r_2^2}\right)\right) \tag{9}$$

where $\mathrm{E}(\cdot)$ is the incomplete elliptic integral of the second kind.

The radii of the curvatures at the incident and scattered diffraction points, $\rho_{1,2}$, are calculated as

$$\rho_{1,2} = \frac{\sqrt{\left(r_1^4 r_2^2 \sin^2\theta_{1,2} + r_1^2 r_2^4 \cos^2\theta_{1,2}\right)^3}}{r_1^4 r_2^4}. \tag{10}$$

The total received field from an ellipse $E^{\mathrm{Rx}}_{\mathrm{Elipse}}$ is calculated as the summation of the reflection and scattered diffraction fields from both sides of the ellipse and the direct field when the LoS is not blocked, and is calculated as only the summation of the scattered diffraction fields when the LoS is blocked as

$$E^{\mathrm{Rx}}_{\mathrm{Elipse}} = \begin{cases} G^{\mathrm{Tx}}G^{\mathrm{Rx}}E^{\mathrm{LoS}} + G^{\mathrm{Tx}}_{\mathrm{C}}G^{\mathrm{Rx}}_{\mathrm{C}}E^{\mathrm{C}} \\ \quad +G^{\mathrm{Tx}}_{\mathrm{R}}G^{\mathrm{Rx}}_{\mathrm{R}}E^{\mathrm{R}}, & (\mathrm{LoS}) \\ \sum_{i=1}^{2} G^{\mathrm{Tx}}_i G^{\mathrm{Rx}}_i E^{\mathrm{C}}_i, & (\mathrm{NLoS}) \end{cases} \tag{11}$$

where $E^{\mathrm{R}}, E^{\mathrm{C}}, G^{\mathrm{Tx,Rx}}$, and $G^{\mathrm{Tx,Rx}}_i$ are the electric field of the reflection and diffraction paths from the ellipse, the antenna gains of the boresight and the directions toward the diffraction paths concerning the Tx and the Rx antennas, respectively.

The creeping diffraction coefficient C can be considered as the absorbing-edge diffraction coefficient D in (5) added with an additional term mentioned in [29] as

$$C = D + \sqrt{M_1 M_2}e^{-\mathrm{j}k_0\widehat{r_m}}\sqrt{\frac{2}{k_0}}p^*\left(\xi^d, q^c_{s,h}\right)e^{-\mathrm{j}\frac{\pi}{4}} \tag{12}$$

with

$$M_{1,2} = \left(\frac{k_0\rho_{1,2}}{2}\right)^{\frac{1}{3}}, \tag{13}$$

$$\xi^d = \left(\frac{k_0}{2}\right)^{\frac{1}{3}}\frac{(r_1 r_2)^{\frac{2}{3}}}{r_2}\left(\mathrm{K}\left(\theta_2|1-\frac{r_1^2}{r_2^2}\right)-\mathrm{K}\left(\theta_1|1-\frac{r_1^2}{r_2^2}\right)\right), \tag{14}$$

$$q^c_{s,h} = -\mathrm{j}\sqrt{M_1 M_2}\left(\frac{\eta_0}{\eta}\right)^{\pm 1} \tag{15}$$

where $p^*(\cdot)$ is the associated Fock-type integral. $q^c_{s,h}$ are the parameters corresponding to the perpendicular (soft) polarization and the parallel (hard) polarization. η_0 and η are the free-space impedance and the surface impedance of the dielectric cylinder, respectively. $M_{1,2}$ and ξ^d are the UTD parameters mentioned in [15]. $\mathrm{K}(\cdot)$ is the incomplete elliptic integral of the first kind, respectively.

When the LoS is not blocked, the diffraction wave specularly reflects on the surface of the ellipse. The reflection point $(r_1\cos\theta_3, r_2\cos\theta_3)$, which satisfies the reflection law, is found on the ellipse numerically. θ_3 is the parameter of the reflection point.

To predict the reflection coefficient, the radius of the curvature at the reflection point is needed. The radius of the curvature at the reflection points, ρ_3, is calculated by (16).

$$\rho_3 = \frac{\sqrt{\left(r_1^4 r_2^2 \sin^2\theta_3 + r_1^2 r_2^4 \cos^2\theta_3\right)^3}}{r_1^4 r_2^4}. \tag{16}$$

The reflection coefficient R can be considered as the edge diffraction coefficient D in (5) added with an additional term mentioned in [29] as

$$R = D + M_3\sqrt{\frac{2}{k_0}}p^*\left(\xi^r, q^r_{s,h}\right)e^{-\mathrm{j}\frac{(\xi^r)^3}{12}}e^{-\mathrm{j}\frac{\pi}{4}} \tag{17}$$

with

$$M_3 = \left(\frac{k_0\rho_3}{2}\right)^{\frac{1}{3}}, \tag{18}$$

$$\xi^r = -2M_3\cos\theta^{\mathrm{inc}}, \tag{19}$$

$$q^r_{s,h} = -\mathrm{j}M_3\left(\frac{\eta_0}{\eta}\right)^{\pm 1} \tag{20}$$

where $q^r_{s,h}$ are the parameters corresponding to the perpendicular (soft) polarization and the parallel (hard) polarization. M_3 and ξ^r are the UTD parameters mentioned in [15]. θ^{inc} is the incident angle.

B. MEASUREMENT SYSTEM

To evaluate the human motion-based prediction of the dynamic HBS channel, the dynamic HBS channel measurement and MoCap measurement should be synchronized. Our measurement system [25] synchronizes the two instruments by an external trigger signal. The external trigger signal is fed to the multi-channel digitizer and the synchronization port of the MoCap cameras respectively, as shown in Fig. 9(a). When the trigger signal is detected by the digitizer, the time, t_0, of the sounder's clock is recorded. On the other hand, the MoCap system starts the recording of each camera immediately when the trigger is detected, as shown in Fig. 9(b). Thus, the time offset from the MoCap system's clock to the sounder's is t_0.

In the dynamic channel measurement, the shadowing gain $G^{\mathrm{S}}_{\mathrm{meas}}(t)$ is calculated as

$$G^{\mathrm{S}}_{\mathrm{meas}}(t) = 10\log_{10}\frac{P^{\mathrm{Rx}}(t)}{P^{\mathrm{LoS}}} \tag{21}$$

where $P^{\mathrm{Rx}}(t)$ and P^{LoS} are the instantaneous received power at time t and the static received power without the human presence, respectively. The channel sounder is built by using a couple of commercial off-the-shelf (COTS) beam-forming antennas (Tx: BFM06005, Rx: RFM06010, Sivers IMA [30]) as the RF front and a multi-channel baseband digitizer [31] at Niigata University, Japan, as shown in Fig. 10. The Tx and Rx antennas are array antennas with 4 by 16 elements and 8

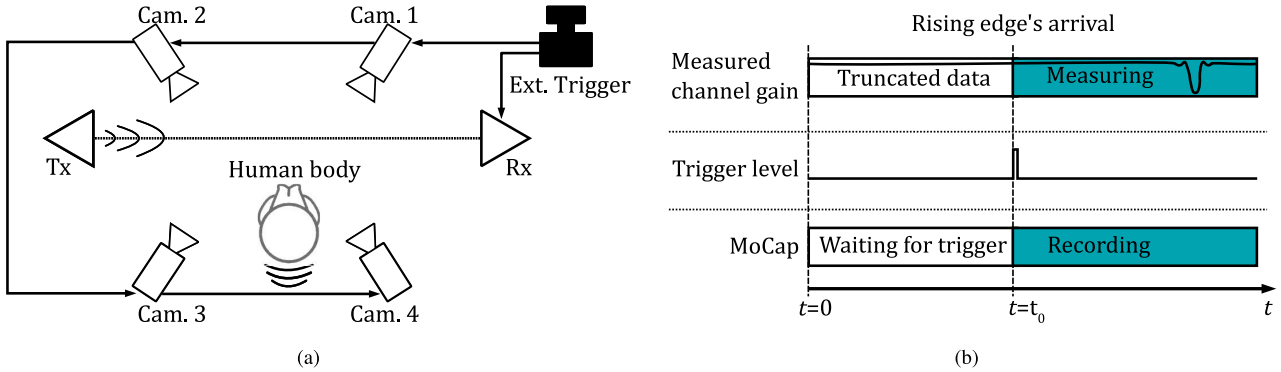

FIGURE 9. The synchronized channel sounder and the MoCap. (a) Hardware architecture. (b) External rectangular pulse and the status of both instruments before and after receiving the trigger signal.

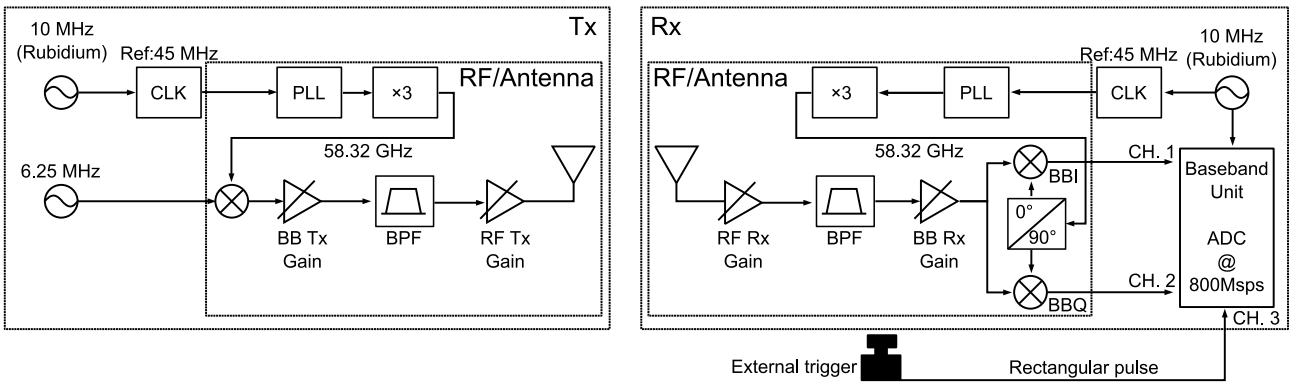

FIGURE 10. Hardware architecture of the channel sounder using COTS beamforming antenna at 58 GHz. The external trigger signal is fed to the third channel when the.

by 16 elements, which form narrow beams. The half-power beam widths (HPBW) of beam patterns are approximately 6° in the azimuth plane. The boresight transmission power is 41 dBm maximum in terms of equivalent isotropic radiated power (EIRP). The carrier wave at 58.32 GHz is heterodyne up-converted by a continuous wave (CW) at 6.25 MHz. After the heterodyne down conversion, the baseband I/Q signals were captured at the digitizer. What we refer to as a channel acquisition is the complex amplitude of the received I/Q signal. The upper tone was separated by using a fast Fourier transform. According to the description of the channel sounder [31], the dynamic range can be calculated from the signal-to-noise ratio (SNR) of the free space measurement and the dynamic range is 39 dB when the antenna separation is 7 m. For the normal walking speed $|v|$ is roughly 1 m/s, the maximum Doppler frequency $\nu_{\max}$ Hz is defined as

$$\nu_{max} = \frac{|v|}{\lambda}\left(\hat{u}_{\mathrm{v}} \cdot \hat{u}_{\mathrm{Tx-p}} + \hat{u}_{\mathrm{v}} \cdot \hat{u}_{\mathrm{p-Rx}}\right) \tag{22}$$

where λ, $\hat{u}_{\mathrm{Tx-p}}$, $\hat{u}_{\mathrm{p-Rx}}$, and $\hat{u}_{\mathrm{v}}$ are the wavelength of the transmitted wave at 58.32 GHz, the unit vector point to the specimen from the Tx, the unit vector point to the Rx from the specimen, and the unit vector of the specimen's velocity, respectively. Regarding the narrow beam width of the antennas, only the propagation paths within the first null positions of the beam pattern, $\phi_{\mathrm{Tx,Rx}}$, are expected to be received. When the specimen walks transverse to the LoS, the maximum of the Doppler frequencies can be estimated by (23).

$$\nu_{max} \leq \frac{2|v|}{\lambda} \cos\left(\frac{\pi - \phi_{\mathrm{Tx,Rx}}}{2}\right). \tag{23}$$

Since $\phi_{\mathrm{Tx,Rx}}$ are 20° [31], the received maximum Doppler frequency $\nu_{\max}$ is estimated not to exceed 68 Hz. To observe the HBS event including the Doppler frequency, the frame rate is set at 680 fps. The specifications of the channel sounder are given in Table 1.

TABLE 1. Specification of the channel sounder.

Carrier frequency	58.32 GHz
Signal bandwidth	12.5 MHz
EIRP	41 dBm
HPBW	Azimuth: 5.6°, Elevation: 45° (Tx), 18° (Rx)
Sounding signal	Unmodulated 2 tone
Sampling rate	40 MHz
FFT length	58752
Frame rate	680 fps
Recording period	20 s

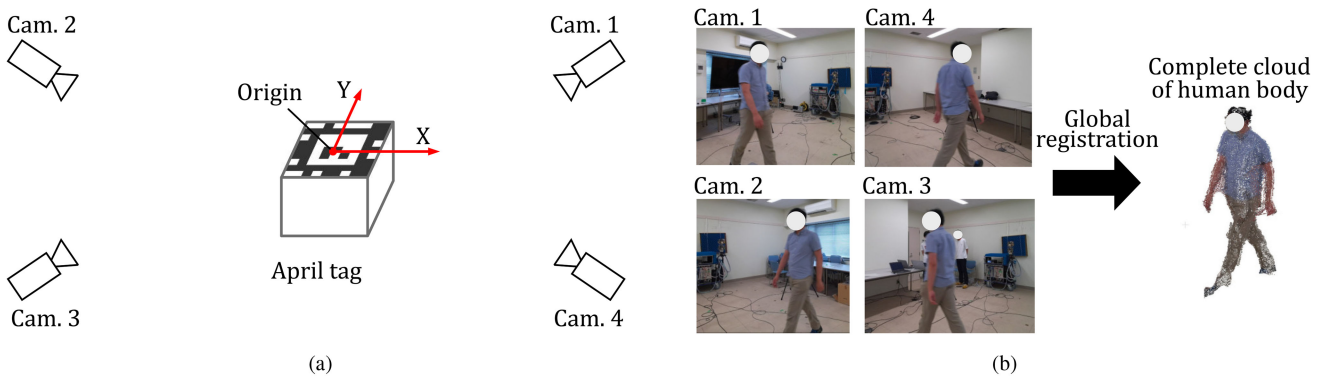

FIGURE 11. Global registration for the four captured PCs. (a) April tag measurement. The tag is used to find the origin and the axes in each camera. (b) Example of global registration.

The MoCap system is composed of four synchronized Azure Kinect DK depth cameras [32]. Using the synchronized infrared (IR) flashlight and the camera, the distance from the depth camera to the surface can be measured as the time-of-flight. The detailed surface of the environment is then recorded as a frame of depth map. From the frames of the depth maps, the PCs of the specimen recorded by four depth cameras are generated. To reconstruct the complete surface of the specimen, the transform matrices are needed to register the local PC to the global coordinate system. Regarding the static setting of the depth cameras, the transform matrices are found by an April tag measurement [33], [34], which is independent of the MoCap for the human body. The April tag is placed at the center of the experiment field, as shown in Fig. 11(a). The position and direction of the April tag are used as the reference to find the transformation matrix between the two depth cameras' local coordinate systems. Using the transform matrices, the four PCs are transferred to the complete PC on the surface of the specimen as shown in Fig. 11(b).

Since the proposed models are generated from the measured point cloud as shown in Section II, the localizing accuracy of the PC-based models' dimension is affected by the random ranging error of the depth camera, which is less than 17 mm in the standard deviation as described in [32]. The Pr-th percentile c_{Pr} in the probability function P(·) of the measured range can be represented as

$$\mathrm{P}(X < c_{Pr}) = Pr \tag{24}$$

where X is the measured value of the dimension of the PC-based model. By assuming that the measured range of the surface distributes Gaussian, the 97.5th percentile of the distribution of the measured range that $Pr = 97.5\%$ can be expressed according to the empirical rule in statistics as

$$c_{Pr} = \mu + \sigma_{\mathrm{model}} \tag{25}$$

where μ and σ_{model} are the population mean and the standard deviation of the dimension of the PC-based model, respectively. Considering there is an angle θ_{M} between the boresight of the depth camera and the line of sight of the TRx

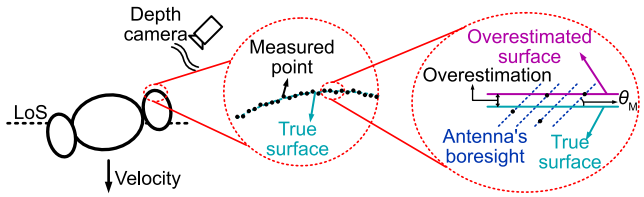

FIGURE 12. The overestimation of the position of the human surface. Since the contour points are the outermost points among their neighbors, the overestimation is the maximum of the ranging error toward the depth antenna.

as shown in Fig. 12, σ_{model} can be related to the standard deviation of the ranging error σ_{range} by (26).

$$\sigma_{\mathrm{model}} = \sigma_{\mathrm{range}} \sin(\theta_M). \tag{26}$$

Since the depth cameras were placed in the four corners, it can be found that $\theta_{\mathrm{M}} = \frac{\pi}{4}$. Finally, with a 97.5% confidence level, the overestimation $c_{97.5}$ of the dimensions of the PC-based models is less than 24 mm.

C. DYNAMIC CHANNEL MEASUREMENT

A simple indoor measurement scenario of a dynamic HBS channel was considered, where a device-to-device (D2D) propagation link was shadowed by a pedestrian walking naturally. The measurement was conducted in an empty meeting room at Niigata University. Since the sounding signal was a CW, the interference of the multi-path components (MPCs) from the environment was excluded by using the narrow beam and deploying absorbers behind the antennas. The set-up diagram is shown in Fig. 13. The Tx and the Rx were deployed at a height of 1.1 m and separated by 6.5 m. In the measurement, the specimen traversed a linear trajectory across the middle of LoS between the Tx and Rx for 1.5 round trips. The first Fresnel radius at the center of the LoS was 85 mm. The thickness of the specimen at 1.1 m height was about 270 mm. The four cameras of the MoCap system were deployed in the four corners where the complete surface of the human specimen can be recorded.

Using the definitions as shown in Fig. 14, The specification of the specimen is identified in Table 2. In [35], [36],

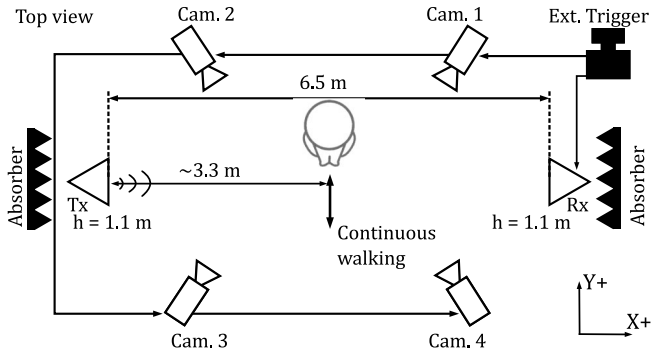

FIGURE 13. Diagram of measurement set-up with human traversing a linear trajectory cross to the LoS between the Tx and Rx.

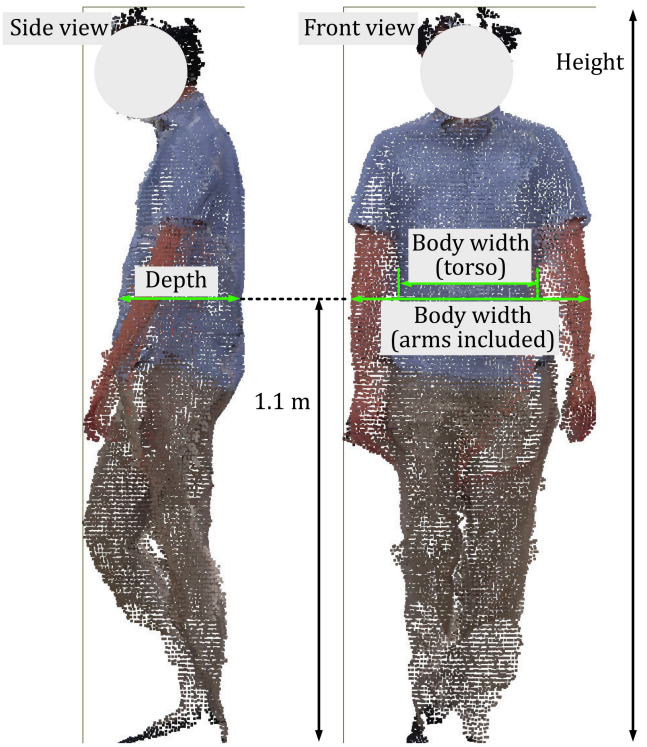

FIGURE 14. The photograph of the specimen with the body dimensions as defined in Table 2.

TABLE 2. Specification of the specimen.

Human subject	Male A
Height	1.72 m
Body depth	0.27 m
Body width (torso)	0.32 m
Body width (arms included)	0.54 m
Cloth	Thin cotton (0.4 mm)

it was confirmed that even the 1 mm thick cotton material contributes attenuation less than 3 dB at mmW band (up to 300 GHz). Thus, the clothing, a thin cotton shirt, in the measurement of this work is considered transparent at

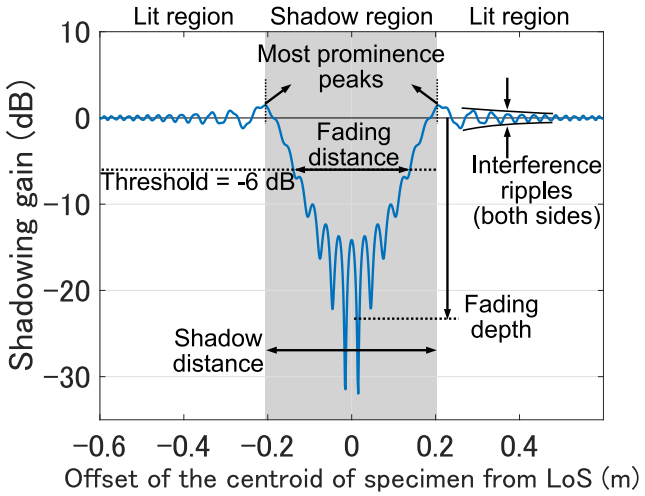

FIGURE 15. The example of the metrics of the propagation channel shadowed by a fixed screen. The shadow distance is defined as the distance between the two most prominent peaks on both sides.

58 GHz. Since the clothing is visible at the IR band, the gap between the clothing and the skin of the specimen may lead to an overestimated surface.

The coverage of the HPBW of the RX antenna beam pattern at the specimen was 0.34 m in the horizontal plane and 1.09 m in the vertical plane. Therefore, the multipath fading caused by the diffracted waves at both sides of the specimen could be measured, while the floor-reflected wave and the diffracted wave at the head of the specimen could not be identified.

IV. RESULTS AND DISCUSSION

Precise localization and capture of the shape of the human body enable a fair comparison between the proposed PC-based human models and the conventional screen model. By using the synchronized system consisting of the channel sounder and the MoCap system, the screen models and the elliptic cylinder model can be generated from the instantaneous human shape, and the conventional screen model can be localized precisely. As mentioned in Section III-B, the possible overestimation of the dimension of the surface of the human body was 24 mm in maximum. In this section, we compare the common fixed screen model using premeasured dimensions of the human body with the proposed screen models and the elliptic cylinder model. The definitions of the metrics are shown in Fig. 15. First, the measurement result and the predictions of the shadow distance are compared quantitatively. In Section IV-A, the shadow distance is defined as the distance between the two most prominent peaks on both sides before and after the shadow event for judging when to switch the communication link. In Section IV-B, the fading distance is defined as the distance between the position of the human body where the shadowing gain drops below the threshold and recovers to indicate how long the communication link is lost. The threshold for the fading distance is defined as -6 dB, which

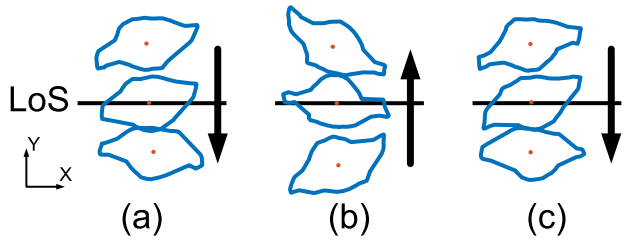

FIGURE 16. The horizontal contour of the specimen in the three measurements. (a) The first outward trip. (b) The return trip. (c) The second outward trip.

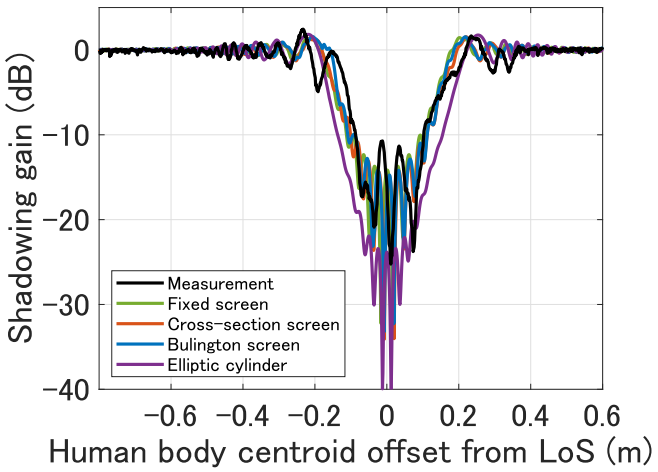

FIGURE 17. The synchronized shadowing gain of the first outward trip.

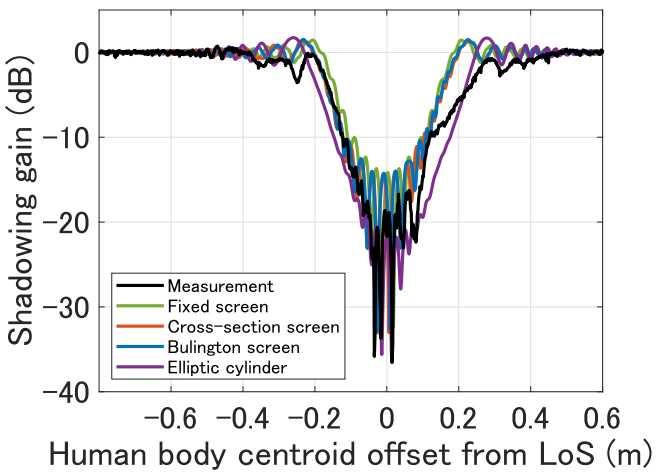

FIGURE 18. The synchronized shadowing gain of the return trip.

is the shadowing gain of the shadow boundary obtained by letting the edge of a semi-infinite screen transverse to the direction of propagation. Next, the agreement of the fading depth and the interference ripples in the lit region are compared. The results of the three MoCap measurements are shown in Fig. 16. In the outward trips, the right arm approached the LoS first while the torso left the LoS last. On the return trip, the torso approached the LoS first while the right arm left the LoS lastly. The results of the shadowing gain are shown in Figs. 17, 18, and 19.

TABLE 3. The shadow distances of the measurement and the predicted results of the dynamic shadowing channel.

Number of trial	1	2	3	MAE
Measurement	470 mm	511 mm	466 mm	-
Fixed screen	413 mm	413 mm	413 mm	69 mm
Cross-section screen	438 mm	463 mm	444 mm	34 mm
Bullington screen	426 mm	454 mm	444 mm	41 mm
Elliptic cylinder	470 mm	539 mm	489 mm	17 mm

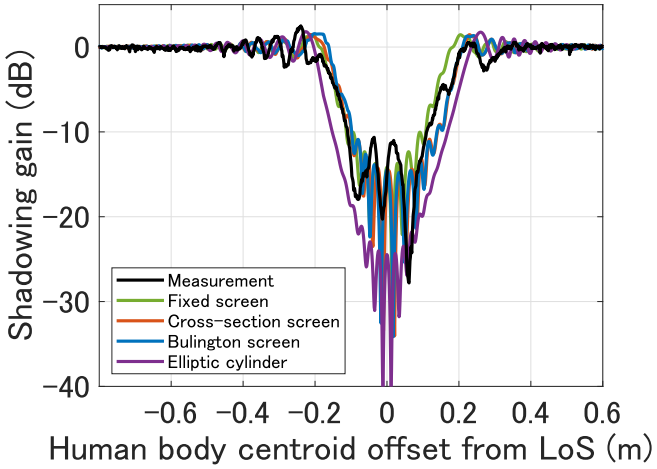

FIGURE 19. The synchronized shadowing gain of the second outward trip.

A. COMPARISON BETWEEN THE MODELS AGAINST THE SHADOW DISTANCE

The shadow distance in the HBS event can be used to judge when to switch the communication link to the alternative path and when to resume. Comparing the screen defined by the premeasured body depth in Table 2 with our proposed screen models and the elliptical cylinder model, we obtain the results in Table 3. In all measurements, the proposed PC-based models outperformed the fixed screen. Compared with the conventional fixed screen model, the mean absolute errors (MAE) of the shadow distances were improved by 51%, 41%, and 75% by using the proposed Cross-section screen, Bullington screen, and elliptic cylinder models, respectively. The proposals succeeded in following the motion of the swinging arm to recognize the cross-section of the human body, which is approaching the first Fresnel zone. In addition, the screen models tended to make false negatives of the shadow event prediction, while the elliptic cylinder model tended to make false positives of the shadow event prediction. Regarding false negatives causing unexpected communication cut-offs, but false positives only degrade the networking efficiency, the proposed elliptic cylinder model is recommended for the proactive scheduling application.

B. COMPARISON BETWEEN MODELS AGAINST THE FADING DISTANCE

The fading distance in the HBS event shows when the communication link is cut off. The results are obtained in

TABLE 4. The fading distances of the measurement and the predicted results of the dynamic shadowing channel.

Number of trial	1	2	3	MAE
Measurement	243 mm	348 mm	277 mm	-
Fixed screen	279 mm	279 mm	279 mm	34 mm
Cross-section screen	273 mm	294 mm	300 mm	36 mm
Bullington screen	275 mm	298 mm	292 mm	32 mm
Elliptic cylinder	340 mm	388 mm	371 mm	77 mm

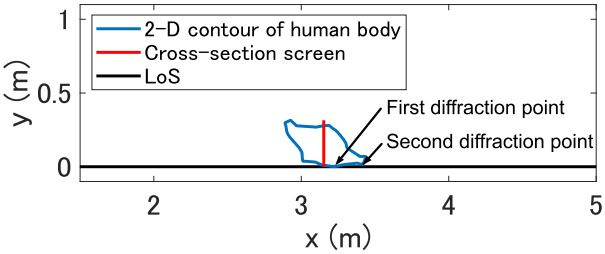

FIGURE 20. The horizontal contour of the human body and the estimated cross-section screen when the centroid of the human body was at 0.17 m in the return trip.

Table 4. Though the improvement of the MAE of the fading distance due to the proposals was not obvious, the predictions using the proposed screen models can follow the changes between the different measurements. On the other hand, the predictions of the elliptic cylinder tend to overestimate the fading distance. When emulating whether the propagation link is cut off by the human body, the proposed cross-screen model and the Bullington model are recommended.

C. COMPARISON BETWEEN MODELS AGAINST THE FADING PATTERNS

The strengths of the creeping wave and the scattering wave from the human body are important to simulate the instantaneous shadowing gain accurately. The accuracy of the predicted creeping wave can be evaluated by observing the agreement of the fading depth, and the accuracy of the scattering wave can be evaluated by observing the agreement of the interference ripple in the lit region. The agreement of the fading depth and the interference ripple were observed from the comparison of the patterns of the shadowing gain between the prediction and the measured results, as shown in Figs. 17, 18, and 19.

When observing the fading depth, the elliptic cylinder model overestimated the fading depth of the outward trips, which the screen models predicted precisely. However, the fading depth of the return trip was correctly predicted by the elliptic cylinder model but underestimated by the screen models. The reason was the disagreement between the ellipse and the horizontal contour. As shown in Fig. 6, there are unmatched surfaces in the gap between the arms and the torso. When the arm approached the LoS first or left the LoS last, the filled surface at the position where there was a gap blocked the Fresnel zone and contributed to a faster decay or a later rise. On the other hand, by observing the horizontal contours in Fig. 16, we can find the disagreement of the fading depths was due to the poor estimation of the creeping length. The creeping lengths along the belly and the back had good agreements to the creeping lengths along an ellipse only when the front direction of the human body was perpendicular to the LoS. In the outward cases, the creeping lengths were overestimated. Since the creeping length contributes to an evanescence term in the UTD calculation in (11), the fading depths were overestimated by the elliptic cylinder model in the two outward trips. The results showed a complex model rather than a simple elliptic cylinder model is needed to predict the creeping wave accurately.

In the decay and rise phases between the LoS and the NLoS conditions, where the centroid of the human body was located between -0.3 to 0.1 and 0.1 to 0.3, the screen models predicted the HBS shadowing gain accurately in most cases. However, there was a significant deviation observed especially in the rising phase of the return trip where the centroid of the body was between 0.1 to 0.3 m, as shown in Fig. 18. To investigate the cause of such occasional prediction errors, the difference between the screen model and the instantaneous posture of the human body when the deviation was exhibited should be observed, as shown in Fig. 20. It was observed that the torso and the right arm were similarly distanced from the LoS and formed a double-diffraction condition. Since additional diffraction contributed to exceeding attenuation, the screen models overestimated the shadowing gain. Such occasionally overestimated shadow gain caused false negatives observed in Section IV-A.

In the observation of the interference ripples in the lit region, it was found the predictions based on the elliptic cylinder model were more accurate compared with the predictions based on the screen models. It showed the scattering wave from the surface of the human body can be modeled as a specularly reflected wave considering the curvature of the surface. Since the discrepancies remained, it suggested that a complex model rather than a simple elliptic cylinder model is needed to predict the reflection wave from the human body accurately.

V. CONCLUSION

This paper proposed three types of PC-based geometric models that fit the instantaneous human body for the deterministic HBS channel model in the indoor (6.5 m) scenario at 58 GHz. Unlike the conventional fixed screen model, the proposals flexibly change their shape and direction to fit the instantaneous cross-section of the obstacle from the antennas' viewpoint. The flexible models took the detailed geometry of the human body into account and enabled the simulation of the deterministic channel propagation affected

by a human with a changing cross-section. To accurately evaluate the proposals, a measurement of the dynamic propagation channel at the 58 GHz band affected by the human body using our synchronized channel sounder and MoCap system was conducted. The shadow distance, fading distance, and the pattern of the shadow gain of the prediction were compared with the measured results. The proposed cross-section screen and the Bullington screen performed well in tracking the change of the shadow distances between the measurements. The proposed elliptic cylinder model improved the prediction of the shadow distance by 75% on average and the scattering waves from the human body. The results showed the proposed PC-based human body model is effective for the dynamic HBS channel simulator. In a simulation where the LoS is shadowed by a complex part of the human body, e.g., the torso and the arm form a gap or a concave structure, the clearance of the Fresnel zone can be misestimated. Since complex-shaped contours are not considered by the proposals in this work, the development of the PC-based 3D human model that accommodates the complex-shaped human body is the future topic.

REFERENCES

[1] "Channel models for IEEE 802.11ay," Inst. Elect. Electron. Eng., Piscataway, NJ, USA, document 802.11-15/1150r2, Sep. 2015.

[2] Y. Ghasempour, C. R. C. M. da Silva, C. Cordeiro, and E. W. Knightly, "IEEE 802.11ay: Next-generation 60 GHz communication for 100 Gb/s Wi-Fi," *IEEE Commun. Mag.*, vol. 55, no. 12, pp. 186–192, Dec. 2017.

[3] J. G. Andrews et al., "What will 5G be?" *IEEE J. Sel. Areas Commun.*, vol. 32, no. 6, pp. 1065–1082, Jun. 2014.

[4] A. W. Mbugua, K. Saito, F. Zhang, and W. Fan, "Characterization of human body shadowing in measured millimeter-wave indoor channels," in *Proc. PIMRC*, 2018, pp. 1–5.

[5] S. Obayashi and T. Fujii, "An OTA measurement setup considering human body shadowing effect for indoor millimeter link in specific floor environment," in *Proc. CAMA*, 2017, pp. 396–399.

[6] A. F. Molisch, "Statistical description of the wireless channel" in *Wireless Communications*, New York, NY, USA: Wiley, 2011, ch. 5, pp. 69–99.

[7] M. Jacob, S. Priebe, M. Peter, and M. Wisotzki, "Fundamental analyses of 60 GHz human blockage," in *Proc. EuCAP*, 2013, pp. 117–121.

[8] A. Deng, Y. Liu, and D. M. Blough, "Exploring performance limits on proactive fair Scheduling for mmWave WLANs," in *Proc. LANMAN*, 2022, pp. 1–6.

[9] Y. Oguma, T. Nishio, K. Yamamoto, and M. Morikura, "Proactive handover based on human blockage prediction using RGB-D cameras for mmWave communications," *IEICE Trans. Commun.*, vol. E99-B, no. 8, pp. 1734–1744, Aug. 2016.

[10] "Azure Kinect body tracking joints." Microsoft. Accessed: Oct. 7, 2022. [Online]. Available: https://learn.microsoft.com/en-us/azure/kinect-dk/body-joints

[11] D. M. Sullivan, *Electromagnetic Simulation Using the FDTD Method*. Piscataway, NJ, USA: IEEE Press, 2013.

[12] C. A. Balanis, *Advanced Engineering Electromagnetics*, 2nd ed. New York, NY, USA: Wiley, 2012.

[13] T. Aoyagi, M. Kim, J. Takada, K. Hamaguchi, and R. Kohno, "Numerical simulations for wearable BAN propagation channel during various human movements," *IEICE Trans. Commun.*, vol. E94-B, no. 9, pp. 2496–2500, Sep. 2011.

[14] *Propagation by Diffraction*, ITU-Rec. P.526-15, Int. Telecommun. Union, Geneva, Switzerland, Oct. 2019.

[15] P. Pathak, W. Burnside, and R. Marhefka, "A uniform GTD analysis of the diffraction of electromagnetic waves by a smooth convex surface," *IEEE Trans. Antennas Propag.*, vol. 28, no. 5, pp. 631–642, Sep. 1980.

[16] E. Plouhinec and B. Uguen, "UTD human body models comparison based on dual motion capture and radio measurements," in *Proc. APWC*, 2019, pp. 192–197.

[17] G. R. MacCartney, S. Deng, S. Sun, and T. S. Rappaport, "Millimeter-wave human blockage at 73 GHz with a simple double knife-edge diffraction model and extension for directional antennas," in *Proc. VTC*, 2016, pp. 1–6.

[18] E. Plouhinec and B. Uguen, "Knife-edge diffraction models for human body shadowing prediction," in *Proc. APWC*, 2022, pp. 36–41.

[19] S. Mukherjee, G. Skidmore, T. Chawla, A. Bhardwaj, C. Gentile, and J. Senic, "Scalable modeling of human blockage at millimeter-wave: A comparative analysis of knife-edge diffraction, the uniform theory of diffraction, and physical optics against 60 GHz channel measurements," *IEEE Access*, vol. 10, pp. 133643–133654, 2022.

[20] U. T. Virk and K. Haneda, "Modeling human blockage at 5G millimeter-wave frequencies," *IEEE Trans. Antennas Propag.*, vol. 68, no. 3, pp. 2256–2266, Mar. 2020.

[21] J. M. Eckhardt, C. E. Reinhardt, T. Doeker, E. A. Jorswieck, and T. Kürner, "Capacity analysis for time-variant MIMO channel measurements at low THz frequencies," in *Proc. EuCAP*, 2023, pp. 1–5.

[22] A. Bhardwaj, D. Caudill, C. Gentile, J. Chuang, J. Senic, and D. G. Michelson, "Geometrical-empirical channel propagation model for human presence at 60 GHz," *IEEE Access*, vol. 9, pp. 38467–38478, 2021.

[23] P. Koivumäki and K. Haneda, "Point cloud ray-launching simulations of indoor multipath channels at 60 GHz," in *Proc. PIMRC*, 2022, pp. 1–7.

[24] K. Saito, N. Keerativoranan, and J. Takada, "Dynamic propagation simulation method from LiDAR point cloud data for smart office scenario," in *Proc. PIMRC*, 2022, pp. 1–6.

[25] C. Kang, X. Du, and J. Takada, "Synchronized dynamic channel sounder and posture capture for millimeter Wave radio channel suffered from human body shadowing," in *Proc. EuCAP*, 2023, pp. 1–5.

[26] K. Bullington, "Radio propagation for vehicular communications," *IEEE Trans. Veh. Technol.*, vol. 26, no. 4, pp. 295–308, Nov. 1977.

[27] C. Gustafson and F. Tufvesson, "Characterization of 60 GHz shadowing by human bodies and simple phantoms," in *Proc. EuCAP*, 2012, pp. 473–477.

[28] J. B. Andersen, "UTD multiple-edge transition zone diffraction," *IEEE Trans. Antennas Propag.*, vol. 45, no. 7, pp. 1093–1097, Jul. 1997.

[29] X. Du and J. Takada, "A uniform additional term using Fock-type integral to unify edge diffraction, creeping diffraction, and reflection in lit and shadowed regions," *Prog. Electromagn. Res. B*, vol. 101, no. 6, pp. 101–117, Jul. 2023.

[30] "Reduce time to market–speed up your mmWave product design using the evaluation kits," Data Sheet EVK06002/00, SIVERS IMA, Gothenburg, Sweden, Accessed: Oct. 7, 2022. https://www.sivers-semiconductors.com/sivers-wireless/evaluation-kits/

[31] M. Kim, S. Tang, and K. Kumakura, "Fast double-directional full azimuth sweep channel sounder using low-cost COTS beamforming RF transceivers," *IEEE Access*, vol. 9, pp. 80288–80299, 2021.

[32] "About Azure Kinect DK." Microsoft. Accessed: Oct. 7, 2022. [Online]. Available: https://learn.microsoft.com/en-us/azure/Kinect-dk/about-azure-kinect-dk

[33] E. Olson, "AprilTag: A robust and flexible visual fiducial system," in *Proc. ICRA*, 2011, pp. 3400–3407.

[34] T. Song. "Extrinsic calibration for multiple Azure Kinect cameras." GitHub Repository. Accessed: Oct. 7, 2022. [Online]. Available: https://github.com/stytim/k4a-calibration

[35] J. E. Bjarnason, T. L. J. Chan, A. W. M. Lee, M. A. Celis, and E. R. Brown, "Millimeter-wave terahertz and mid-infrared transmission through common clothing," *Appl. Phys. Lett.*, vol. 85, no. 4, pp. 519–521, Apr. 2004.

[36] G. Sacco, D. Nikolayev, R. Sauleau, and M. Zhadobov, "Antenna/human body coupling in 5G millimeter-wave bands: Do age and clothing matter?" *IEEE J. Microw.*, vol. 1, no. 2, pp. 593–600, Apr. 2021.

CHECHIA KANG (Member, IEEE) was born in 1995. He received the B.E. degree in international development engineering and the M.S. degree in transdisciplinary science and engineering from the Tokyo Institute of Technology, Tokyo, Japan, in 2019 and 2021, respectively, where he is currently pursuing the D.E. degree.

From 2019 to 2023, he was a Research Assistant with the School of Environment and Society, Tokyo Institute of Technology. His research interests include numerical electromagnetic simulation and measurements of the human shadowing effect.

Mr. Kang is a student member of the IEICE, Japan.

XIN DU (Member, IEEE) was born in 1992. He received the B.E. degree in international development engineering and the M.S. and D.E. degrees in transdisciplinary science and engineering from the Tokyo Institute of Technology, Tokyo, Japan, in 2017, 2019, and 2022, respectively.

From 2017 to 2019, he was a Research Assistant with the School of Environment and Society, Tokyo Institute of Technology, where he was a Postdoctoral Researcher with the School of Environment and Society from 2022 to 2023. He is currently an Assistant Professor with the Graduate School of Sciences and Technology for Innovation, Yamaguchi University, Japan. His research interests include wireless communication, diffraction theory, and reconfigurable intelligent surfaces.

Dr. Du received the 2023 IEEE AP-S Japan Young Engineer Award in 2023. He is a member of the IEICE, Japan.

JUN-ICHI TAKADA (Senior Member, IEEE) received the B.E., M.E., and D.E. degrees in electrical and electronic engineering from the Tokyo Institute of Technology, Tokyo, Japan, in 1987, 1989, and 1992, respectively.

He was a Research Associate with Chiba University, Chiba, Japan, from 1992 to 1994, and an Associate Professor with the Tokyo Institute of Technology from 1994 to 2006. He was also a Researcher with the National Institute of Information and Communications Technology, Kanagawa, Japan, from 2003 to 2007. He has been a Professor with the Tokyo Institute of Technology since 2006. His research interests include radio-wave propagation and channel modeling for mobile and short-range wireless systems, regulatory issues of spectrum sharing, and ICT applications for international development.

Prof. Takada is a Fellow of IEICE, Japan.